

Comparing Local Starbursts to High-Redshift Galaxies: a Search for Lyman-Break Analogs

Sara M. Petty,^{1,2} Duília F. de Mello,^{1,2,3} John S. Gallagher III,⁴ Jonathan P. Gardner,²
Jennifer M. Lotz,⁵ C. Matt Mountain,⁶ Linda J. Smith^{6,7,8}

ABSTRACT

We compare the restframe far-ultraviolet (FUV) morphologies of 8 nearby interacting and starburst galaxies (Arp 269, M 82, Mrk 08, NGC 0520, NGC 1068, NGC 3079, NGC 3310, NGC 7673) with 54 galaxies at $z \sim 1.5$ and 46 galaxies at $z \sim 4$ in the Great Observatories Origins Deep Survey (GOODS) images taken with the Advanced Camera for Surveys onboard the Hubble Space Telescope. We calculate the Gini coefficient (G), the second order moment of 20% of the brightest pixels (M_{20}), and the Sérsic index (n). We find that 20% (11/54) of $z \sim 1.5$ and 37% (17/46) of $z \sim 4$ galaxies are bulge-like, using G and M_{20} . We also find $\sim 70\%$ of the $z \sim 1.5$ and $z \sim 4$ galaxies have exponential disks with $n > 0.8$. The 2D profile combined with the nonparametric methods provides more detail, concerning the nature of disturbed systems, such as merger and post-merger types. We also provide qualitative descriptions of each galaxy system and at each redshift. We conclude that Mrk 08, NGC 3079, and NGC 7673 have similar morphologies as the starburst FUV restframe galaxies and Lyman-break galaxies at $z \sim 1.5$ and 4, and determine that they are Lyman-break analogs.

Subject headings: galaxies: evolution – galaxies: high-redshift – galaxies: interactions – galaxies: structure – ultraviolet: starburst

1. Introduction

Deep images of the universe have shown that many of the progenitors of present-day galaxies are experiencing very active star formation and undergoing violent gravitational interactions. However, the method by which interactions in youthful galaxies drive their baryonic structures is still

an open issue. Moreover, it is still not clear in which respects the star formation processes at high-redshift, differ from current galaxies. One way of trying to visualize how these processes influence our view of the distant universe is by artificially placing local interacting and starburst galaxies at high- z and comparing their properties with observed high- z objects.

Pinpointing a definite redshift for the formation of the Hubble sequence is difficult, even though a few observational studies suggest that it occurred in the redshift range $1 < z < 2$ (Conselice et al. 2004; Papovich et al. 2005). The color dispersion, size and luminosity of galaxies from $z \sim 3$ to ~ 1 are important gauges of galaxy evolutionary processes. Papovich et al. (2005) find that the mean galaxy size, of UV-bright galaxies, increases by 40% from $z \sim 2.3$ to ~ 1 and that characteristic sizes have not changed since $z \sim 1$. They also find that the color dispersion is higher for galaxies at $z \sim 1$, than for galaxies at $z \sim 3$, implying a lack

¹Department of Physics, The Catholic University of America, Washington, DC 20064; sara.m.petty@nasa.gov

²Observational Cosmology Laboratory, Code 665, Goddard Space Flight Center, Greenbelt, MD 20771

³Johns Hopkins University, Baltimore, MD 21218

⁴Department of Astronomy, University of Wisconsin-Madison, 475 North Charter Street, Madison, WI 53706

⁵National Optical Astronomical Observatory, 950 N. Cherry Ave., Tucson, AZ 85719

⁶Space Telescope Science Institute, 3700 San Martin Dr., Baltimore, MD 21218

⁷ESA Space Telescope Operations Division, MD 21218, USA

⁸Department of Physics and Astronomy, University College London, Gower Street, London WC1E 6BT, UK

of older stellar populations in the higher redshift galaxies.

Lyman-break galaxies (LBGs) are $z \gtrsim 2.5$ galaxies selected by FUV-dropout (see Steidel et al. 1996) in the spectral energy distribution. The Lyman-break line occurs predominately in hot, young stellar atmospheres. Comparison spectra of LBGs with local starburst galaxies have shown remarkable similarities in metallicities (Giavalisco 2002). The UV luminosities and star-formation rates are significantly larger ($\sim 100 L_{1500}$) for LBGs than for local starburst galaxies (Giavalisco 2002). This raises questions about how the morphologies of LBGs resemble local starburst galaxies, and how the evolution of primeval galaxies leads to the Hubble sequence observed today.

Several studies have also searched for local analogs to LBGs. Hoopes et al. (2007) used stellar mass ratios, surface brightness and luminosity plots to find ultraviolet luminous galaxies (UVLGs; $L > 2 \times 10^{10} L_{\odot}$) that fit the typical LBG surface brightness profile. According to Heckman et al. (2005), LBG analogs are very compact, with large surface brightnesses ($L > 10^8 L_{\odot} \text{ kpc}^{-2}$), but this does not tell us whether these systems have multiple clumps, or single bulges, nor do they determine the type of surface brightness profile.

A study by Burgarella et al. (2007) analyzed LBGs at $z \sim 1$ using GALEX and Spitzer/MIPS data to establish the SED properties of blue LBGs and red LBGs. The authors define red and blue LBGs by the dust attenuation $A_{FUV} = 2.5$ and 1.5, respectively. They further state that the blue LBGs, based on color selection, have low dust attenuation, and that there are suggestions of a small population of “dusty” LBGs at high redshift. The luminosity functions for both red and blue LBGs are similar, and they use this as a warning for relying strictly on color selection to determine the properties of star-forming galaxies.

Overzier et al. (2008) analyzed 8 UVLGs, artificially redshifted them and determined that they fit the morphological quantities for high- z starburst galaxies. A primary difference between the Overzier et al. (2008) study and the one we present is that their sample represents objects that are LBGs at $z = 0$, while we observe how morphological analysis can be biased due to redshifting, using local starburst galaxies of different types and lower luminosities. We also used 2D profiling,

which can distinguish brightness distributions and star-forming clumps that might be missed through nonparametric methods.

Lotz et al. (2006) use the Gini coefficient (G), the second order moment of 20% of the brightest pixels (M_{20}), and concentration (C) morphology analysis to classify rest-frame FUV galaxies at $z \sim 1.5$ and 4 with GOODS and UDF images. The authors created a noise-free de Vaucouleurs bulge and exponential disk to use as benchmarks with the $z \sim 1.5$ and 4 samples. They find that $\sim 30\%$ of the LBGs are bulge-like in their morphologies and $\sim 50\%$ have values closer to a merger or postmerger. Their results are roughly in agreement with hierarchical model predictions for merger rates at high redshifts in Somerville et al. (2001), because the $z \sim 1.5$ sample has more extended star-forming disks than the $z \sim 4$ sample. Quantitative studies, such as the kinematic, non-parametric and 2D profiles of high- z objects are difficult to obtain and to make true comparisons with nearby objects because of resolution and low S/N levels compared with the local counterparts. Artificially redshifting local galaxies is a way to place local galaxies at a similar resolution and conduct morphological studies.

One of the first attempts at artificially redshifting starburst UV restframe galaxies was done by Hibbard & Vacca (1997). The authors use B-, and V-band images to simulate the HDF at $z \sim 0.5 - 2.5$. They particularly look at peculiar galaxies and find that the tidal features from these disturbed galaxies are still viewable at high- z . They do not apply evolutionary effects, such as luminosity or size evolution to their sample. They warn of the biases of measuring morphologies for $z > 1.5$ systems, since only the regions that have been least extinguished are detected. With recent observations, such as GOODS/ACS, better resolution has been achieved and can resolve more of these features, but caution should still be taken in determining distributions of stellar populations. Focusing on the FUV is a method of purposefully biasing the sample toward bright star-forming regions to find similarities with the high- z FUV-bright galaxies and LBGs.

Ravindranath et al. (2004, 2006) established surface brightness profiles, using the Sérsic index (n), and ellipticities of high- z galaxies. In Ravindranath et al. (2006), they conducted a mul-

tiwavelength study on GOODS images and identified ~ 4700 LBGs and 292 starburst galaxies at $z \sim 1.2$. Exponential profiles comprised about 40% of the LBGs, while $\sim 30\%$ have steep, $r^{1/4}$ -like, profiles and $\sim 30\%$ have disturbed morphologies.

In this study, we present the morphologies of 8 FUV, starburst galaxies, using G , M_{20} , and the Sérsic index, n , and we compare the values of these objects with GOODS $z \sim 1.5$ and 4 FUV restframe galaxies. We used the GALEX FUV-band to artificially redshift our sample, because LBGs are FUV-selected. A key difference in our study is that we include a combination of non-parametric and 2D analysis to base our conclusions of LBG analog candidacy. Other studies have focused on one type of method to derive standards by which to classify galaxies (eg. Lotz et al. 2006; Ravindranath et al. 2006; Overzier et al. 2008). We combine both methods for a more complete quantitative analysis. In §2 and §3, we describe our sample and approach to simulating high redshifts. In §4 we show, in detail, the analysis techniques used to quantitatively classify the morphologies, and §5 provides the results of our study. Finally, we conclude with our key discoveries in §6. We have adopted the cosmological constants $H_0 = 70 \text{ km s}^{-1} \text{ Mpc}^{-1}$, $\Omega_m = 0.3$, and $\Omega_\Lambda = 0.7$ throughout this paper.

2. Galaxy Sample

Our sample consists of the following: three interacting galaxies with well extended HI tidal tails from Hibbard et al. (2001) –Arp 269, M 82, NGC 3079; three starburst galaxies with varied morphologies –Mrk 08, NGC 3310, NGC 7673; and two galaxies from Lotz et al. (2006) –NGC 0520, NGC 1068 for comparison with Lotz et al. results. We use the GALEX FUV sky-subtracted images provided by Multimission Archive at STScI (MAST). Figures 1-a and 2-b show the optical (Sloan Digital Sky Survey (York et al. 2000), or Digitized Sky Survey as labeled) and GALEX FUV. We artificially redshifted GALEX FUV images for all galaxies. In the case of M 82, we also included ACS F435W (B_{435}) artificially redshifted to $z \sim 1.5$, which corresponds with observations in the ACS F850L (z_{850}). The sky images for simulating the ACS F435W, F555W (V_{555}), F775W (i_{775}) and F850L, were taken from empty sky re-

gions in the GOODS field. We describe the artificial redshift process in § 3.1. We provide general information for our objects in Table 1.

We obtained 10, $z \sim 1.5$ galaxies from the Voyer et al. (2008) U-band catalog to compare with the artificially redshifted sample. We chose objects with photometric redshifts $0.8 \lesssim z \lesssim 1.8$ and created GOODS/ACS B_{435} -band cutouts from MAST.

The other comparison sample of $z \sim 1.5$ and 4 galaxies comes from Lotz et al. (2006). We included 55 objects from the GOODS North and South fields in the redshift range $1.2 < z < 1.8$. The other galaxies are GOODS South $z \sim 4$ LBGs. We acquired the GOODS/ACS B_{435} -, V_{555} -, z_{850} - and i_{775} -band images of these objects from MAST.

3. Artificial Redshift Simulations

We used the GALEX FUV images to artificially redshift local starburst galaxies to $z \sim 1.5$ and 4 as if they were observed in the GOODS/ACS B_{435} - and $V_{555}+i_{775}$ -bands. A section of background sky in the GOODS field for each of the bands was cut and added to the artificially redshifted object. We describe the method in the following subsections.

3.1. Size and Luminosity Evolution

In order to properly redshift FUV images, we used the size-evolution relation discussed in Ferguson et al. (2004), and luminosity function for FUV galaxies measured by Arnouts et al. (2005). For size-evolution, $z \sim 4$ objects have a half-light radii reduction of ~ 0.4 . To accomplish this, we determined the rebinning factor, N_{highz} , which has the form

$$N_{highz} = N_{lowz} * \sigma * n \quad (1)$$

where N_{lowz} is the number of pixels in the original low redshift image, n is the size-evolution factor (we use 0.4 for $z \sim 4$), and σ is the scale ratio determined by

$$\sigma = \frac{\theta_{lowz}}{\theta_{highz}} \frac{\phi_{lowz}}{\phi_{highz}}, \quad (2)$$

where θ_{lowz} and θ_{highz} are the angular sizes for low and high- z , and ϕ_{lowz} and ϕ_{highz} are the pixel scales for their respective redshifts (see Giavalisco

et al. 1996; Lotz et al. 2006). The angular size is the angular distance in kpc per arcsec dependent on redshift. We do not apply any size evolution to $z \sim 1.5$ images.

The luminosity evolution for restframe FUV galaxies with $z \sim 1.5$ to 4 gives a change in magnitude, $\Delta M \sim -3$, since the star formation rates of earlier galaxies is much higher than in the present day. To apply this to the image to be redshifted, we needed to find the value to multiply, or boost, the original, low- z image. For $\Delta M = -3$ the boosting factor becomes ~ 15 .

We multiplied the CPS (counts per second) by this amount for both the $z \sim 1.5$ and 4 images. For artificially redshifting M 82 using ACS B₄₃₅ to z_{850} (simulating $z \sim 1.5$) we boosted the magnitudes by $\Delta M \sim -1$. This accounted for the luminosity evolution in the general population at high- z in the optical rest-frame (see Ravindranath et al. 2004; Barden et al. 2005; Cameron & Driver 2007).

To artificially redshift nearby galaxies to higher redshifts, the original images are sky subtracted, then rebinned by the size and scale ratios discussed above and boosted by the appropriate factor. The resulting image is then added to a background sky image created from an empty region in the GOODS B₄₃₅-, or V₅₅₅+i₇₇₅-bands (Giavalisco et al. 1996; Lotz et al. 2006; Overzier et al. 2008).

4. Morphological Analysis

We used SExtractor (Bertin & Arnouts 1996) for object detection and to create object segmentation maps with a detection threshold set to 0.6σ . The object centers, and Petrosian radius were then used to determine the Gini coefficient and M_{20} , and to create GALFIT models. We defined $1.5r_p$ (r_p is the Petrosian radius at $\eta = 0.2$, where η is the fraction to average surface brightness) as the object radius, following the method by Lotz et al. (2006). For a benchmark, Lotz et al. (2006) created a noise-free de Vaucouleurs bulge and exponential disk and find: $G = 0.6$ and $M_{20} = -2.47$ for the bulge; and $G = 0.473$ and $M_{20} = -1.80$ for the exponential disk.

4.1. The Gini Coefficient

One way to quantitatively determine the bulge-like nature of galaxies is through nonparametric

analysis, such as G , and M_{20} (e.g. Abraham 2003; Lotz et al. 2004), where the primary goal is to identify merging and interacting galaxies. The Gini coefficient is correlated with concentration and surface brightness. The Gini coefficient is defined as

$$G = \frac{1}{|\bar{X}|l(l-1)} \sum (2i-l-1)|X_i|. \quad (3)$$

The sum is from i to l , where \bar{X} , X_i , and l are the mean flux, the rank ordered pixel flux values, and total number of pixels in the object map, respectively. For $G = 1$, all of the light resides in one pixel, and for $G = 0$ all of the light is evenly distributed between the pixels. According to Lotz et al. (2004), typical Gini coefficient values are: ~ 0.35 to 0.55 for mergers; ~ 0.55 to 0.65 for bulge-dominated morphological types.

4.2. M_{20}

M_{20} is a logarithmic ratio between the second order moment of 20% of the brightest pixels and the total flux. Therefore, the more negative value for M_{20} , the more bulge-like the object. M_{20} is defined by

$$M_{20} \equiv \log \frac{\sum_i M_i}{M_{tot}}, \quad (4)$$

where M_i is given by

$$M_i = X_i[(x_i - x_c)^2 + (y_i - y_c)^2]. \quad (5)$$

M_{tot} is the sum from i to l , and x_c , and y_c are the object centers in the x and y position. M_i is summed over the 20% brightest pixels. Typical M_{20} values are approximately -0.8 to -1.1 for mergers, and -1.7 to -2.2 for bulge-dominated morphological types.

4.3. Sérsic 2D modeling

Another morphological analysis method is through 2D modeling, such as the Sérsic index, n , which fits a range of distributions from exponential disks ($n = 1$) to $r^{1/4}$ spheroids ($n = 4$). We used GALFIT software (Peng et al. 2002) to model 2D profiles with the Sérsic index. When n is large, the inner profile is steep and the outer profile is extended. When n is small, the inner profile is shallow and has a steep cut-off at a large radius. Monte Carlo simulations by Ravindranath et al. (2006) give $\langle n \rangle = 3.83$ for spheroids, and

$\langle n \rangle = 1.1$ for disks, which allows for the broad classification scheme of $n > 2.5$ for spheroids, and $n < 2.5$ for disks. Another scheme with typical values for n are: $n < 0.8$ for mergers/LBGs; $0.8 < n < 2.5$ for exponential systems; $n > 2.5$ for bulge systems (Ravindranath et al. 2006).

5. Results

Figures 1, 2, and 3 show the artificially redshifted sample and the resulting GALFIT model images. In Figures 1 and 2, the four columns divide the data by (from left to right): (a) DSS or SDSS color composite images; (b) GALEX FUV; (c) simulation of ACS-B $z \sim 1.5$; (d) simulation of ACS-V₅₅₅+i₇₇₅ $z \sim 4$. M 82 was artificially redshifted with two different wavelength images, to emphasize the change in morphology from UV to optical. We artificially redshifted the ACS-B image into the z_{850} -band as shown in columns (b) and (c).

The object name, morphological parameters G , M_{20} , n , and r_p are displayed in Table 2 for each artificially redshifted object. Every parameter has three listings for the separate redshifts, described by the superscripted z_0 , $z_{1.5}$, and z_4 . The errors for G and M_{20} are based on Lotz et al. (2006), using S/N. Errors for n are based on Ravindranath et al. (2006), where the error is determined by effective radius, and magnitude of a disk ($n < 2.5$) or spheroid ($n > 2.5$). Note the scale change between the $z \sim 1.5$ and $z \sim 4$ images. We have included $1''$ ($1'$) rulers on the $z \sim 1.5$ and $z \sim 4$ ($z \sim 0$) images to highlight this difference.

We discuss each nearby starburst object separately in §5.1, and provide the quantitative results for each redshift ($z \sim 0, \sim 1.5, \sim 4$) in §5.2 and §5.3, we also explain how we determined the LBG analogs in §5.3.

5.1. Artificially Redshifted Starburst Galaxies

The properties of the galaxies in Figures 1 and 2 and the comparison objects in Figure 4 are qualitatively described below.

Arp 269: This is an interacting minor merger which we selected from Hibbard et al. (2001). It consists of the interaction between NGC 4485 and NGC 4490 with an extended HI tail where

tidal effects can be seen. The GALEX FUV image clearly shows the two separate galaxies. As the system is redshifted to $z \sim 4$, SExtractor does not deblend the two galaxies, and is detected as a single object.

M 82: This strong starburst galaxy is part of the M 81 interacting triplet (M 81, M 82, and NGC 3077) and is also listed in Hibbard et al. (2001). The HI tidal tail is well extended from M82. It has very different characteristics in the FUV compared with the optical. The optical image looks like a typical edge-on galaxy. The FUV has a clover pattern, due to the hot wind cones coming from the nucleus, making it difficult to measure the surface brightness of the disk. These cones are visible in H α . It is barely resolved in the artificially redshifted images, because of the low S/N of the GALEX FUV image. The extended gas disappears within the noise and leaves a small, peculiar shaped object. The optical continues to look like an edge-on in the B₄₃₅- to z_{850} -band redshift image, while the restframe FUV becomes almost indistinguishable from the background as it is redshifted.

Mrk 08: This merging pair is very blue, with the two galaxies (three bright knots) visible in the DSS composite image. It is classified as a Wolf-Rayet galaxy, which suggests a very young burst (4-6 Myr; Esteban & Méndez 1999). The FUV image does not resolve the separate galaxies, and the appearance stays similar for each redshift. This object is one of the LBG analogs we have identified. We discuss the morphological analysis, leading to this result in the follow section.

NGC 0520: This galaxy is an irregular galaxy with peculiar UV morphology. It is considered an intermediate-state merger (Hibbard & van Gorkom 1996). Lotz et al. (2006) artificially redshifted this galaxy and found it to be a merger-dominated system. We find that the high- z simulations look very similar to tadpole galaxies that are observed in intermediate and high- z deep HST images (Elmegreen et al. 2005; de Mello et al. 2006). The peculiar UV features do not appear in the high- z images, and the brightest part is a small knot off-center of a diffuse extension.

NGC 1068: This is a spiral galaxy with a bright nucleus (AGN) and tightly wound spiral arms

that extend into fainter arms, forming a ring structure in the FUV. It is another galaxy artificially redshifted by Lotz et al. (2006). The arms and ring are lost in the high- z images, and the nucleus becomes more spherically shaped at $z \sim 4$.

NGC 3079: This edge-on galaxy is a Seyfert 2 galaxy. It has a bright bulge and is interacting with two other galaxies (NGC 3073 and MCG +09-17-009). The interacting pair has extended HI only along NGC 3079 (Hibbard et al. 2001). The redshifting process changes the appearance of “clumpiness,” so that in both the $z \sim 1.5$ and 4 it looks like a chain galaxy with multiple knots and no bulge. We have also determined this to be a LBG-like object, based on the quantitative results described in the next sections.

NGC 3310: This spiral galaxy appears irregular in the FUV. Two of the arms form loops in the upper and lower sides of the bulge; they can almost be resolved in the $z \sim 1.5$ and 4 images. Even though it is a spiral like NGC 1068, it has a much younger population, as can be seen from the color composite image. At $z \sim 4$ NGC 3310 has nearly identical morphology to NGC 1068. The peculiar spiral structure is lost at high- z .

NGC 7673: This is a Markarian starburst galaxy (Mrk 325) with a large blue clump, surrounded by smaller clumps to the left, in a winding pattern. In the FUV, the galaxy looks highly compact with little detail resolved. As it is artificially redshifted, the galaxy continues to look more spherical. It is similar to Mrk 08 in this regard. We also have determined this to be a LBG analog.

5.2. Comparison Galaxies

We chose three nearby objects from our sample that we considered to have LBG properties and made a comparison with similar galaxies from the $z \sim 1.5$ and B-dropout GOODS comparison samples. Figure 4 shows six GOODS comparison galaxies, two for each nearby object (from left to right, Mrk 08, NGC 3079, and NGC 7673). The top (bottom) row displays $z \sim 1.5$ B_{435} -band ($z \sim 4$ $V_{555}+i_{775}$ -band) images. We list the morphological parameters G , M_{20} , n , and Petrosian radius (r_p) on the image.

Comparison Objects: The six GOODS restframe FUV objects in Figure 4 resemble the

objects we consider to be LBG-like. We provide the G , M_{20} , n and r_p values for each. They were chosen by similarity in G and M_{20} first, and then visually. All objects are from the Lotz et al. (2006) sample, except for the NGC 3079 analog at $z \sim 1.5$, which is from Voyer et al. (2008).

5.3. GALFIT Models

The images in Figure 3 depict the 2D Sérsic index GALFIT models with the residuals below. All FUV images show structure in the residual images. As the galaxies are redshifted, only a few bright knots remain in the residuals. This is helpful for determining small structure that otherwise might not be detected in the original image. In most of the sample, these knots are the same in $z \sim 1.5$ and 4. In particular, Mrk 08 has two knots that are the brightest parts of the two merging galaxies. NGC 1068 reveals one of the tightly wound arms in $z \sim 1.5$ and the nucleus in both $z \sim 1.5$ and 4. NGC 3079 has three bright knots that are clear in each residual image. NGC 3310 and NGC 7673 reveal the faint, extended components that appear as background in the original images.

It was difficult to fit M 82 in the GALEX FUV as a single galaxy, so we used three components, where one component covers the hot wind cones coming from the nucleus. The other two components fit along the nearly edge-on disk. The Sérsic index values along the disk are very similar, so we averaged them for analysis.

5.4. Morphologies

The values for G , M_{20} , and n are plotted in Figures 5, 6, and 7. The shaded regions delineate systems that are merger- or bulge-dominated. These include the ranges $0 > M_{20} > -1.1$, and $-1.7 > M_{20} > -2.5$ (see Lotz et al. 2004), respectively. We observe, in Figure 5, that most high- z objects, in the comparison high- z samples, fall within the intermediate region, this is consistent with Lotz et al. (2006). The regions, merger and bulge, are based on a small number (4) of local galaxies in Lotz et al. (2006), and it is possible that these should be revised based on a larger sample. Our artificially redshifted objects range from mostly merger-dominated in the FUV to intermediate in both the B_{435} and $V_{555}+i_{775}$. Figures 6 and 7 display the plots of M_{20} and G

with n . Figure 6 is most helpful because the regions for merger- and bulge-dominated systems, are shown along with the vertical line for $n = 0.8$, which marks the LBG cutoff. Everything in the intermediate- and merger-dominated region and less than the $n = 0.8$ line, should be considered an LBG-like candidate.

Lotz et al. (2006) find that 30% of the GOODS LBG ($z \sim 4$; 11/36) and emission-line ($z \sim 1.5$; 16/54) galaxies are bulge-like, based on $M_{20} < -1.6$ and $G \geq 0.55$. We find, using the same criteria, that 20% (11/54) of $z \sim 1.5$ and 37% (17/46) of $z \sim 4$ galaxies are bulge-like. If one looks at Sérsic index, using $n > 0.8$ as the region for exponential profiles (the same criteria as Ravindranath et al. (2006)), one gets $\sim 70\%$ for $z \sim 1.5$ and $z \sim 4$. The majority of these have $M_{20} > -1.6$, implying multiple nuclei, but with an exponential Sérsic index. The higher n value could be due to $S/N < 15$ for all objects, where Ravindranath et al. (2006) claim that n is higher in GOODS than HUDF images for $S/N < 15$. This can cause multiple clumps to no longer be associated as the sky blends with the galaxy, this would lead to a higher n . It is clearly important to rely on more than just one method of quantifying the profiles for these galaxies.

Only two objects remain in the same morphology region from $z=0$ to 4 in Figure 5. NGC 1068 (E in Figures 5-7) stays in the bulge-dominated region, which is expected since it is a nearly face-on spiral. NGC 3079 (F in Figures 5-7) stays in the merger-dominated region, which is due to the three distinct knots observed in the GALFIT residual images (see Figure 3). The comparison objects for NGC 3079, in Figure 4, reside in the merger-dominated area, and are also edge-on galaxies. NGC 3079, and its comparison galaxies, are not mergers, and this discrepancy exposes a weakness in the technique. G - M_{20} values of edge-on galaxies might be misleading due to clumpy/chain morphology.

Upon further inspection of Figure 5, we observe that NGC 3310 (G in Figures 5-7) and NGC 7673 (H in Figures 5-7) move from the edge of the merger-dominated region at $z=0$. NGC 3310 moves into the bulge-dominated section at $z \sim 1.5$ and back to the intermediate region at $z \sim 4$. The residual image, in Figure 3, shows the change in the central bulge for each redshift range. NGC 7673 stays within the intermediate region, shift-

ing slightly in M_{20} , and the residual image shows that the two bright, off-center knots appear in each redshift. Mrk 08 is an object that moves from a merger-dominated system to well within the intermediate region as it is redshifted. In the residual, the FUV has four bright knots that slowly disappear as it is redshifted, leaving two bright knots close to the geometric center. Arp 269 (A, A*) is very peculiar and a special case since it “merges” into one object at $z \sim 4$. The residual images reveal that the two galaxies become very smooth compared with the numerous starburst clumps in the FUV, leaving little residual structure.

In the Sérsic- M_{20} and G plots (Figures 6 and 7), we note that most of the FUV nearby sample is below the $n = 0.8$ line. NGC 1068 (E) is, again, consistently in the bulge-dominated area as it is redshifted. Although, it is important to mention that NGC 1068 moves progressively from a strong exponential profile toward the border of the $n = 0.8/M_{20} = -1.7$ line as it is redshifted. This is most likely due to the profile obtaining a steep cutoff with the applied size-evolution as it is redshifted to $z = 4$ (see §3.1). NGC 1068 is a good standard for testing the morphology of exponential and bulge types at different redshifts. Oppositely, Mrk 08 (C) is consistently in the LBG, merger to postmerger region and we consider it a nearby LBG analog. As it is redshifted it moves into the postmerger area, with a smoother G profile, but it is still within the LBG population. We also consider NGC 7673 (H) and NGC 3079 (F) as LBG analogs. NGC 3079 changes Sérsic morphology from an exponential to LBG type, but remains in the merger region in terms of G and M_{20} . The three bright knots, discussed in the previous section, are what drives the G - M_{20} classification and n becomes shallower due to the loss of the fringe light distribution in the background. The comparison objects for NGC 3079 in Figure 4 also have distinct, multiple knots in their residual images (not shown) and have $n < 0.8$.

6. Summary

We use our GALEX FUV sample of nearby galaxies to simulate galaxies in the GOODS/ACS B₄₃₅- and V₅₅₅+i₇₇₅-bands and determine their properties to compare with high- z samples from Voyer et al. (2008), and Lotz et al. (2006).

We approached the issue of finding nearby LBG analogs by applying luminosity and size evolution on FUV images, since LBGs are FUV-selected. This is different than stating that high- z interacting galaxies are to have the same properties as nearby interacting galaxies. We are looking for morphology types based on what we know from the detailed resolution of nearby galaxies, changing them to simulate high- z objects, and extrapolating morphologies based on the high- z objects observed by ACS in the GOODS field. Can we tell the types of galaxies and interactions that are occurring at high- z using this process? Is the narrow n profile, simply due to shallowness of observations with the loss of resolution at high- z ?

1. We find three objects that have similar morphologies as the starburst FUV restframe galaxies and LBGs from $z \sim 1.5$ to 4: Mrk 08, NGC 3079 and NGC 7673.
2. Mrk 08 is a two galaxy system in the process of merging. It is in the merger area for $z \sim 1.5$ and slips into the intermediate region as it is redshifted to $z \sim 4$. It stays below $n = 0.8$ in the Sérsic plot, which indicates the merger-LBG-type profile. This is consistent with the very young age of this starburst (LBGs are young starbursts). Nearby galaxies similar to Mrk 08 are worth studying in more detail to help determine the environments of primeval galaxies, such as LBGs.
3. NGC 3079 is an edge-on galaxy that stays in the merger- and postmerger-dominated regions in Figure 5 for all redshifts. It has a narrow Sérsic index in the high- z images, which is expected for LBGs, but also likely because of its edge-on, clumpy features. It has an exponential distribution in the FUV image. Edge-on starburst galaxies are also important to consider possible morphological biases, due to orientation.
4. NGC 7673 is a peculiar spiral galaxy that has strong FUV emission and a fairly smooth G and M_{20} distribution of light. It stays in the LBG regions for G , M_{20} and n throughout the redshifting process. The two bright knots in the residual images (see Figure 3) are possible star-forming clumps along spiral arms, which get treated as multiple nuclei.
5. The morphologies vary greatly for many galaxies in each redshift. For example, each galaxy in the Arp 269 interacting system begins in the merger-dominated region. As it is redshifted to $z \sim 1.5$, the system moves toward the bulge-dominated region. The ability to distinguish between the two is lost at $z \sim 4$ and is treated as a single galaxy at which point it slips back into the merger-dominated region, but its Sérsic index remains in the merger-dominated region.
6. We use two different wavelength images to artificially redshift M 82. We use GALEX FUV and ACS B₄₃₅-band images for $z \sim 0$. The G , M_{20} and n morphologies are similar at $z \sim 0$ and at $z \sim 1.5$. This Sérsic index value is questionable, due to the wind cones in the FUV that dominate and were difficult to fit in a 2D profile. This is an example of how multiple wavelength analysis can provide a more cohesive, overarching morphology. M 82 is also a nearly edge-on galaxy, and, as discussed for NGC 3079, this presents issues that should be taken into consideration as well.
7. The narrow n index was tested by Ravindranath et al. (2006) and they found that the opposite case held for a GOODS-UDF comparison: the lower S/N GOODS images tended to have a higher n value for $S/N < 15$. We also test this by placing nearby galaxies, of varying morphologies, and artificially redshift them to high- z . It seems that most of the galaxies do not “stay” in their respective n regions. We find that much caution must be used in comparing quantitative studies of nearby objects with high- z objects.
8. Our analysis displays a primary importance of combining the 2D profile with nonparametric methods: it can identify LBG, or disturbed profiles and possible biases because of orientation (such as in the edge-on case with NGC 3079), where the G and M_{20} might not be as distinguishable.
9. At this time it is difficult to determine what types of interactions occur at high- z using this method, although it is possible with

residual 2D images to get a closer look at the dominating surface features in the fit.

10. It is clear that a larger sample of local galaxies is needed to classify galaxies using the M_{20} , G and n relations. Using multiple rest-frame wavelengths will help to distinguish the biases due to color by cross-matching samples. A survey performed by the James Webb Space Telescope (JWST) (Gardner et al. 2006) would observe the optical rest-frame at high- z . The predictions we obtained in this paper can be tested by such a survey.

We are grateful to S. Ravindranath for discussions concerning luminosity evolution and for the GALFIT tutorial. We also thank B. Holwerda for conversations about SExtractor and morphological analysis, and C. Peng for assistance with GALFIT. The GALEX and GOODS data in this paper were obtained from MAST at the Space Telescope Science Institute (STScI). STScI is operated by the Association of Universities for Research in Astronomy, Inc., under NASA contract NAS5-26555. Support for MAST for non-HST data is provided by the NASA Office of Space Science via grant NAG5-7584 and by other grants and contracts. DSS data were obtained using the Aladin interactive sky atlas (Bonnarel et al. 2000). The Digitized Sky Survey was produced at the Space Telescope Science Institute under U.S. Government grant NAG W-2166. SDSS data were obtained from the SDSS archive Data Release Six. Funding for the SDSS and SDSS-II has been provided by the Alfred P. Sloan Foundation, the Participating Institutions, the National Science Foundation, the U.S. Department of Energy, the National Aeronautics and Space Administration, the Japanese Monbukagakusho, the Max Planck Society, and the Higher Education Funding Council for England.

REFERENCES

- Abraham, R.G., van den Bergh, S., & Nair, P. 2003 *ApJ*, 588, 218
- Arnouts, S., et al. 2005, *ApJ*, 619, L43
- Barden, M., et al. 2005 *ApJ*, 635, 959
- Bertin, E., & Arnouts, S. 1996, *A&AS*, 117, 393
- Bonnarel, F., et al. 2000, *A&AS*, 143, 33
- Burgarella, D., Le Floch, E., Takeuchi, T.T., Huang, J.S., Buat, V., & Rieke, G.H. 2007, *MNRAS*, 380, 986
- Cameron, E., & Driver, S.P. 2007, *MNRAS*, 377, 523
- Conselice, C., et al. 2004, *ApJ*, 600, L139
- de Mello, D.F., Wadadekar, Y., Dahlen, T., Casertano, S., Gardner, J.P. 2006, *AJ*, 131, 216
- de Vaucouleurs, G., de Vaucouleurs, A., Corwin, H.G., Buta, R.J., Patural, G., & Fouqué, P. 1991, *Third Reference Catalogue of Bright Galaxies*, Springer-Verlag (New York)
- Elmegreen, D.M., Elmegreen, B., Rubin, D., & Schaffer, M.A. 2005, *ApJ*, 631, 85
- Esteban, C., & Méndez, D.I. 1999, *A&A*, 348, 446
- Ferguson, H.C., et al. 2004, *ApJ*, 600, L107
- Gardner et al. 2006, *Space Sci. Rev.*, 123, 485
- Giavalisco, M., Livio, M., Bohlin, R. C., Macchetto, F.D., & Stecher, T. P. 1996, *AJ*, 112, 369
- Giavalisco, M. 2002, *ARA&A*, 40, 579
- Gil de Paz, A., et al. 2007, *ApJS*, 173, 185
- Heckman, T.M., et al. 2005, *ApJ*, 619, L35
- Hibbard, J.E., & van Gorkom, J.H. 1996, *AJ*, 111, 2
- Hibbard, J.E. & Vacca, W.D. 1997, *AJ*, 114, 1741
- Hibbard, J.E., van Gorkom, J.H., Rupen, M.P., & Schiminovich, D. 2001, in *Gas and Galaxy Evolution*, ed. J. E. Hibbard, J. H. van Gorkom, & M. P. Rupen (San Francisco: ASP), 657
- Hoopes, C.G., et al. 2007, *ApJS*, 173, 441
- Lotz, J.M., Primack, J., & Madau, P. 2004, *AJ*, 128, 163

- Lotz, J.M., Madau, P., Giavalisco, M., Primack, J., & Ferguson, H.C. 2006, *ApJ*, 636, 592
- Madau, P., Ferguson, H.C., Dickinson, M.E., Giavalisco, M., Steidel, C.C., & Fruchter, A. 1996, *MNRAS*, 283, 1388
- Overzier, R., et al. 2008, *ApJ*, 677, 37
- Papovich, C., Dickinson, M., Giavalisco, M., Conselice, C.J., & Ferguson, H.C. 2005, *ApJ*, 631, 101
- Peng, C.Y., Ho, L.C., Impey, C.D., & Rix, H.-W. 2002, *AJ*, 124, 266
- Ravindranath, S., et al. 2004, *ApJ*, 604, L9
- Ravindranath, S., et al. 2006, *ApJ*, 652, 963
- Somerville, R.S., Primack, J.R., & Faber, S.M. 2001, *MNRAS*, 320, 504
- Steidel, C.C., Giavalisco, M., Pettini, M., Dickinson, M., & Adelberger, K.L. 1996, *ApJ*, 462, L17
- Voyer, E.N., de Mello, D.F., Quirk, C., Siana, B., Teplitz, H., Gardner, J.P. 2008, *AJ*, submitted
- York, D.G., Adelman, J., Anderson, J.E., et al. 2000, *AJ*, 120, 1579

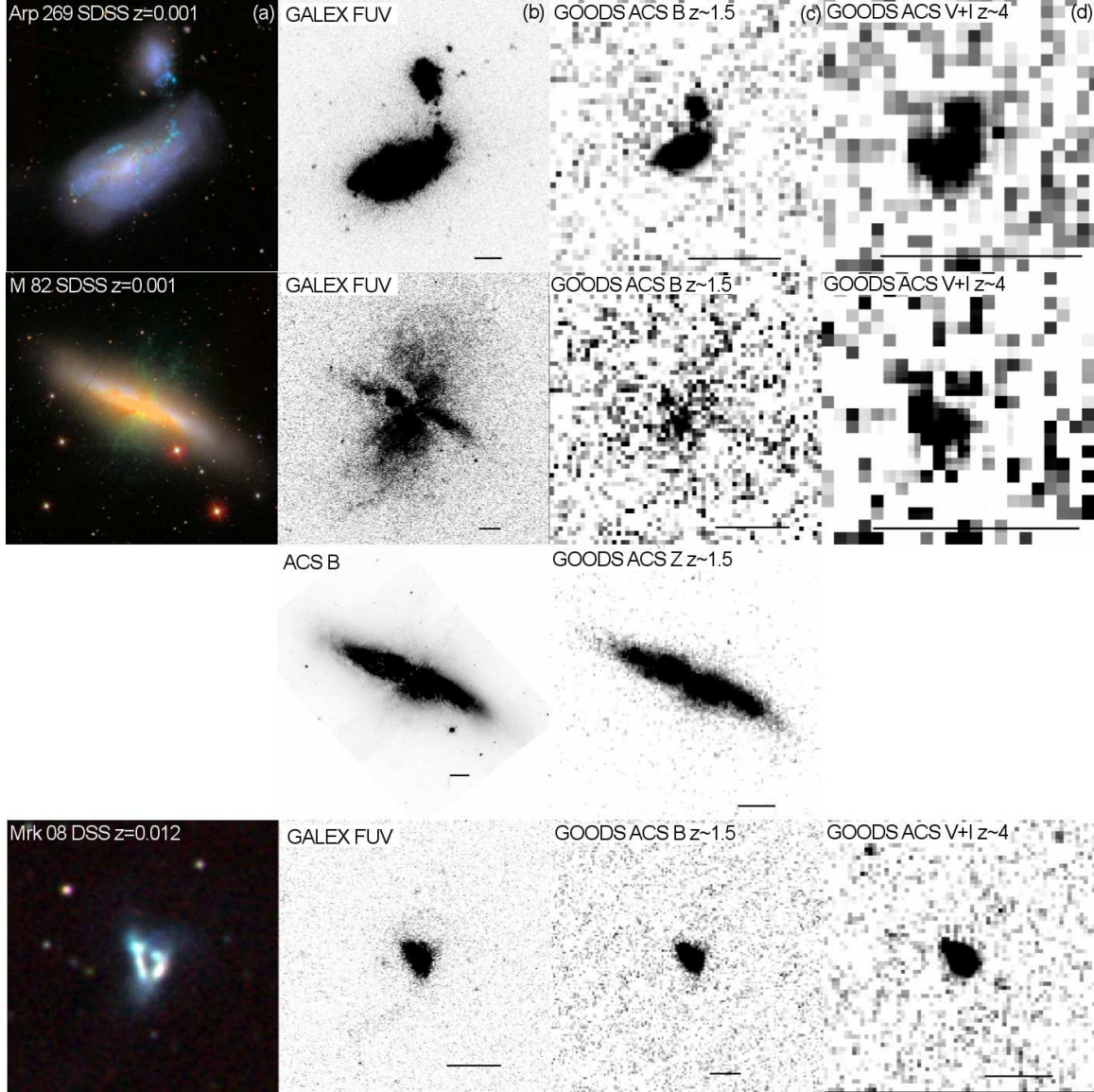


Fig. 1.— Artificially redshifted sample. The columns are as follows (except in the case for M82 B-band): a) color composite optical image from SDSS or DSS, as labeled, the original redshift is listed; b) GALEX FUV image (ruler marks 1'); c) artificially redshifted to $z \sim 1.5$ made to simulate GOODS B_{435} observations (ruler marks 1''); d) artificially redshifted to $z \sim 4$ made to simulate GOODS $V_{555} + i_{775}$ observations (ruler marks 1'').

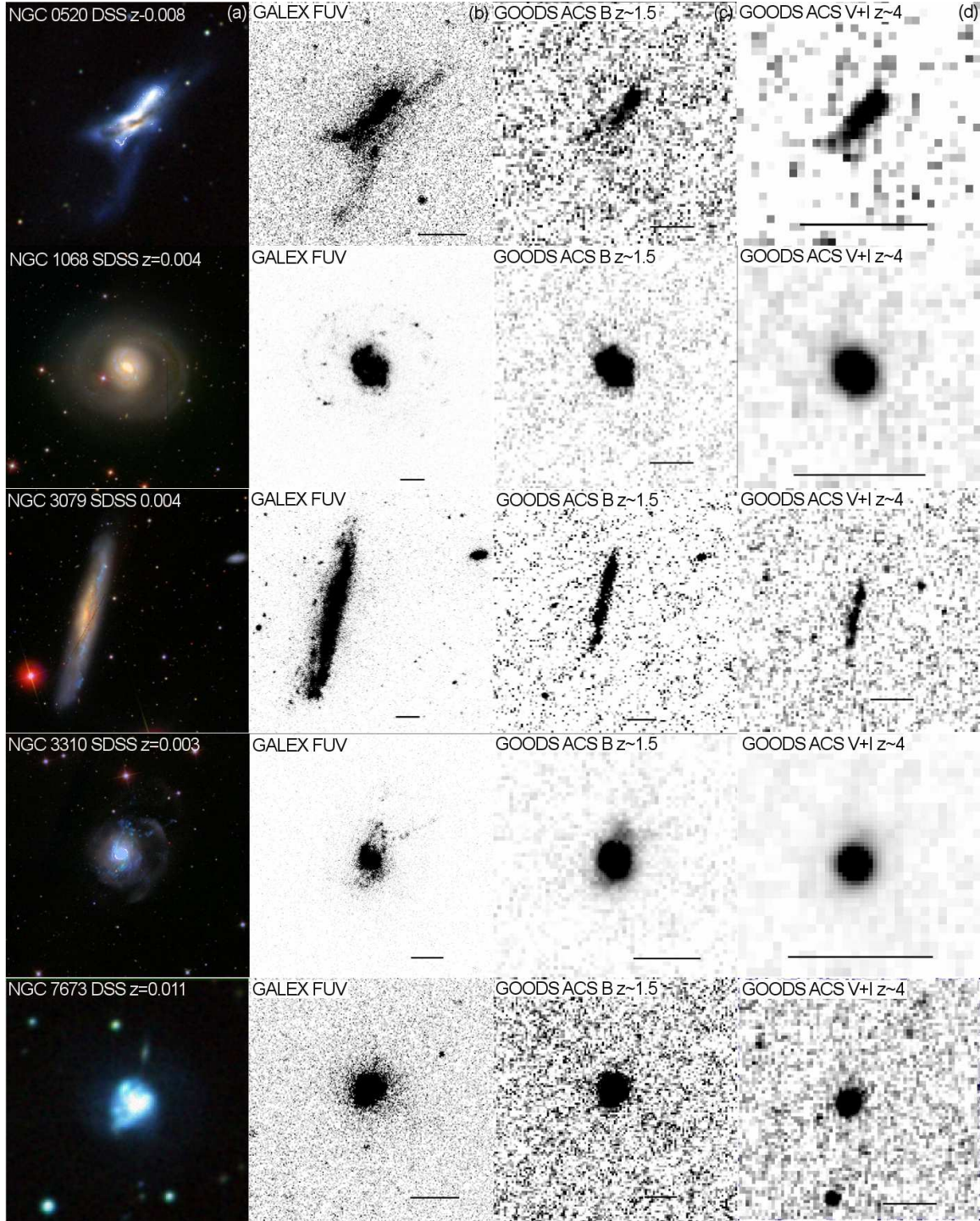


Fig. 2.— Artificially redshifted sample. See Figure 1 for an explanation.

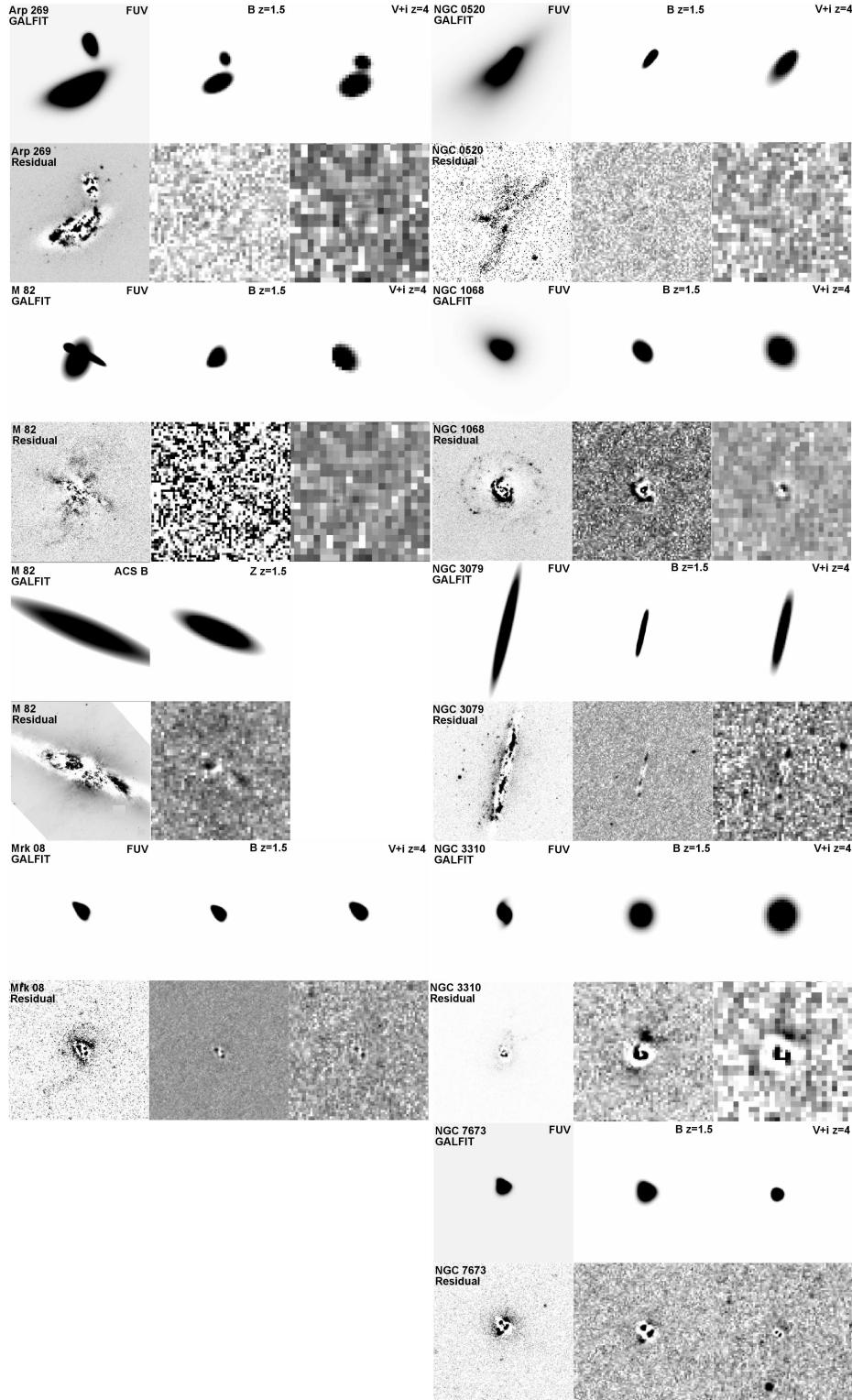


Fig. 3.— GALFIT models for each artificially redshifted object. The GALEX FUV, GOODS B₄₃₅, and GOODS V₅₅₅+*i*₇₇₅ are labeled on the model fit image (M 82 ACS B₄₃₅, and GOODS *z*₈₅₀ are labeled accordingly.). Each object has a top and bottom row, which show the 2D model (top) and the residual image (bottom).

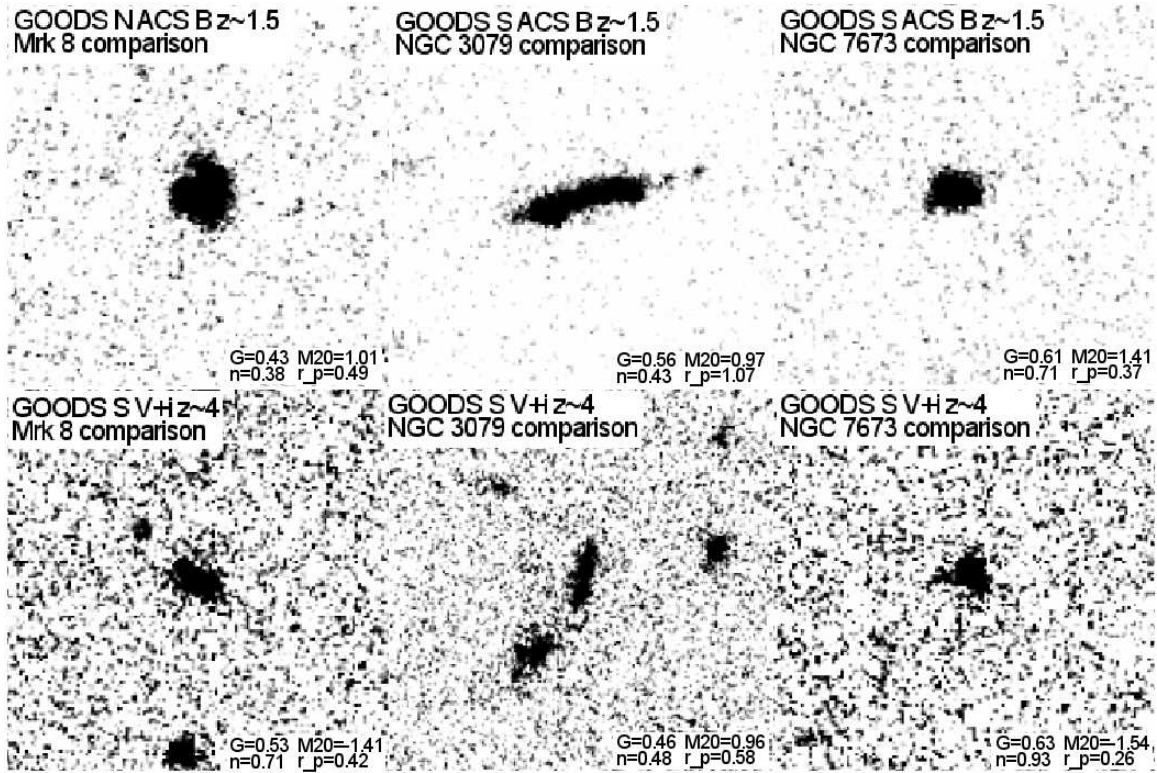


Fig. 4.— Selected objects from the GOODS comparison sample that closely resemble Mrk 08, NGC 3079, and NGC 7673 at the simulated redshifts. The Gini, M_{20} , n , and r_p values are listed on the bottom of each image. For $z \sim 1.5$ (~ 4 , B-dropouts) we used GOODS/ACS $B_{435}(V_{555}+i_{775})$ images. The sample was taken from Lotz et al. (2006) for all except the NGC 3079 $z \sim 1.5$ comparison, which is from Voyer et al. (2008).

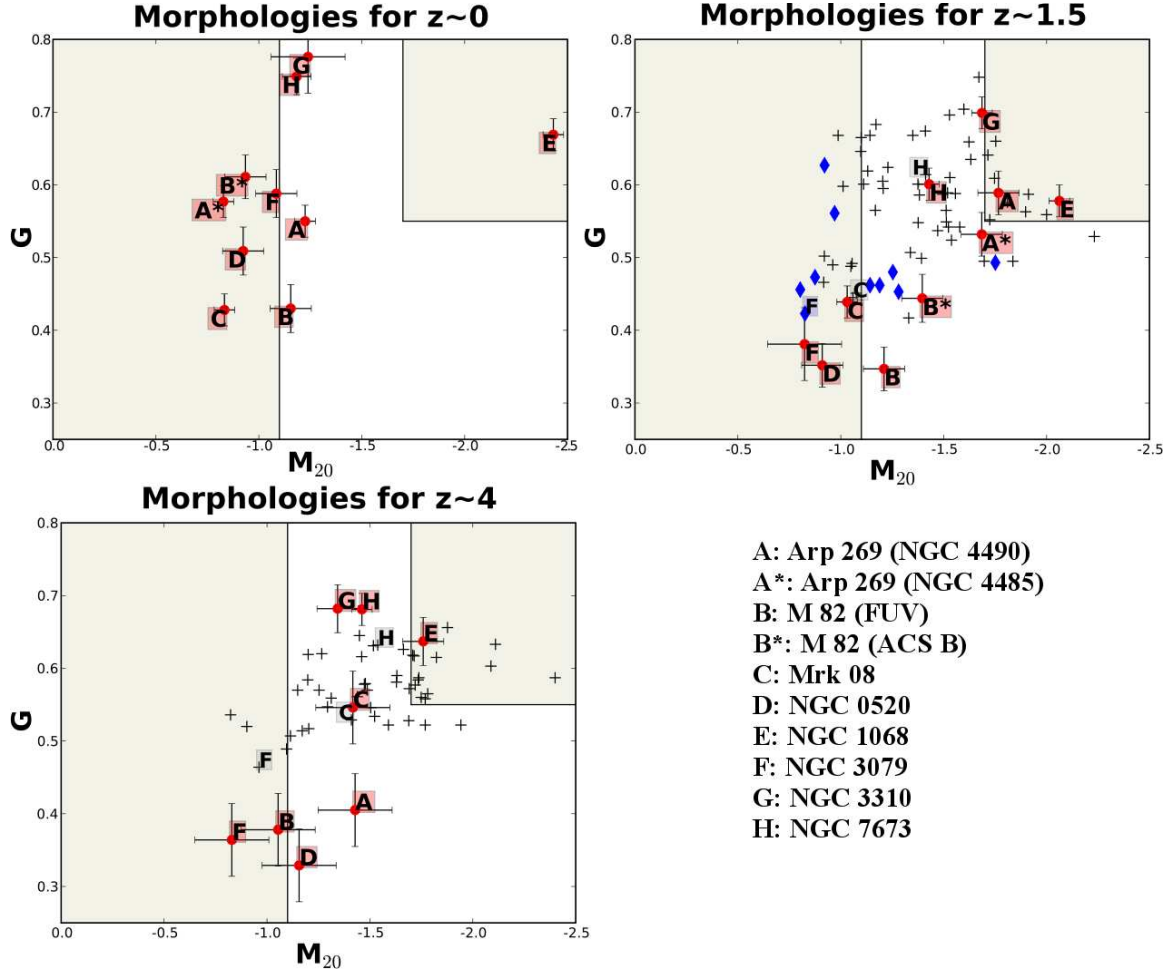


Fig. 5.— Morphologies using Gini, and M_{20} . The red circles indicate the sample used to artificially redshift. The black crosses are the GOODS/ACS sample from Lotz et al. (2006) in the B_{435} -band for $z \sim 1.5$ and $V_{555}+i_{775}$ -bands for $z \sim 4$. The blue diamonds are GOODS-ACS B_{435} -band objects from Voyer et al. (2008). The comparison objects are flagged with the letter-symbol that corresponds with the artificially redshifted objects C (Mrk 08), F (NGC 3079), and H (NGC 7673). The far top left shows the morphologies for the original GALEX FUV images. The top right and bottom left plots show the morphologies for $z \sim 1.5$ and 4, respectively. The shaded regions $0 < M_{20} < -1.1$ and $-1.7 < M_{20} < -2.5$ distinguish between merger- and bulge-dominated galaxies. Error bars are based on Lotz et al. (2006) Fig. 1. The FUV objects tend to be in the merger-dominated region. The $z \sim 1.5$ and 4 objects show a more diverse morphology as they shift into the intermediate region. We find that 20% (11/54) of $z \sim 1.5$ and 37% (17/46) of $z \sim 4$ galaxies are bulge-like.

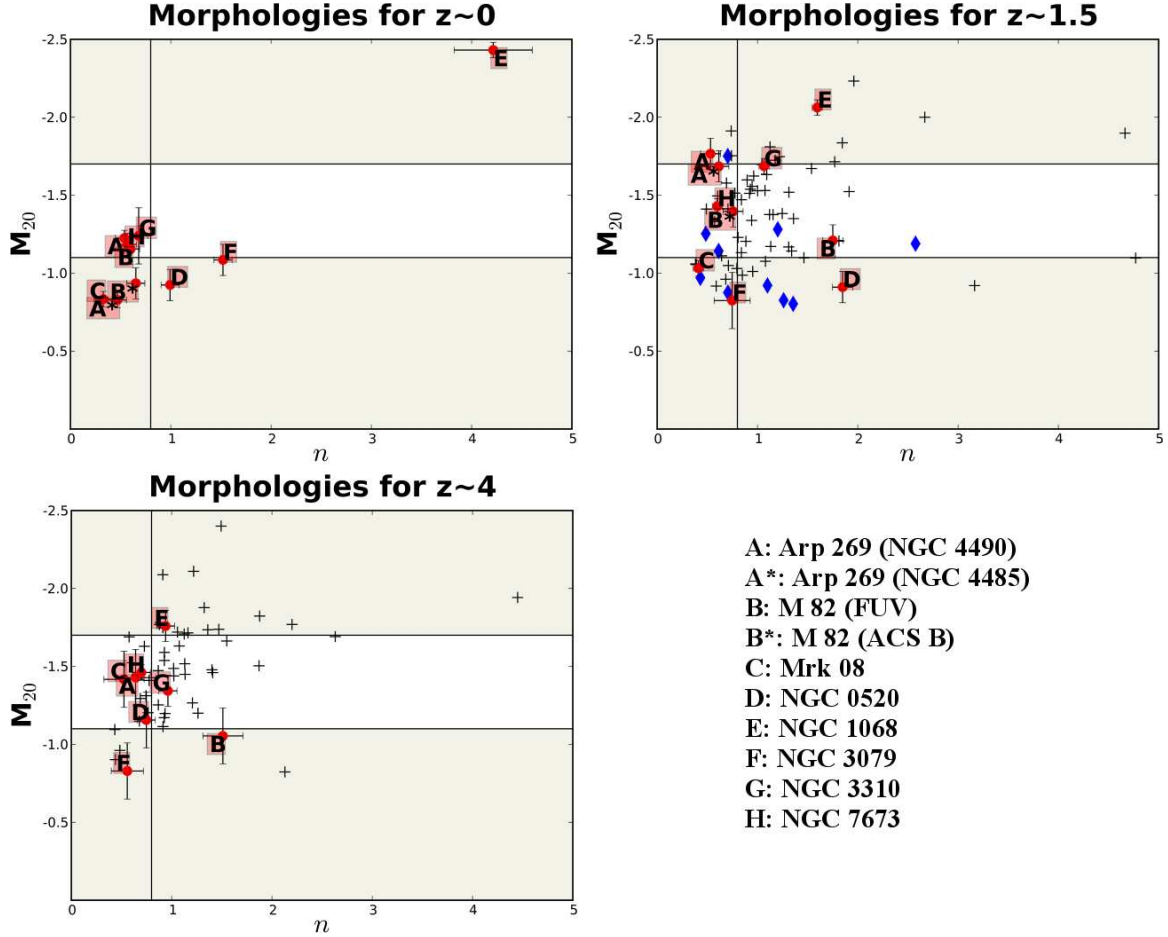


Fig. 6.— We plot M_{20} and n , Sérsic index, to determine LBG-like galaxies. The symbols are the same as for Figure 5. The shaded regions $0 < M_{20} < -1.1$ and $-1.7 < M_{20} < -2.5$ distinguish between merger- and bulge-dominated galaxies. The vertical line marks $n = 0.8$, which helps distinguish whether the object, if to the left of the line, has a LBG profile. The error bars for n values are based on Ravindranath et al. (2006). We note that 7 of the 10 galaxies are below $n = 0.8$ in the FUV and move to various locations in the plot as the systems are redshifted. NGC 1068 (E) is especially noteworthy, because it moves from an exponential profile to right along the border of the $n = 0.8/M_{20} = -1.7$ line as it is redshifted. We determine that Mrk 08, NGC 7673 and NGC 3079 are LBG-types based on their morphologies presented in this figure and in Fig. 5.

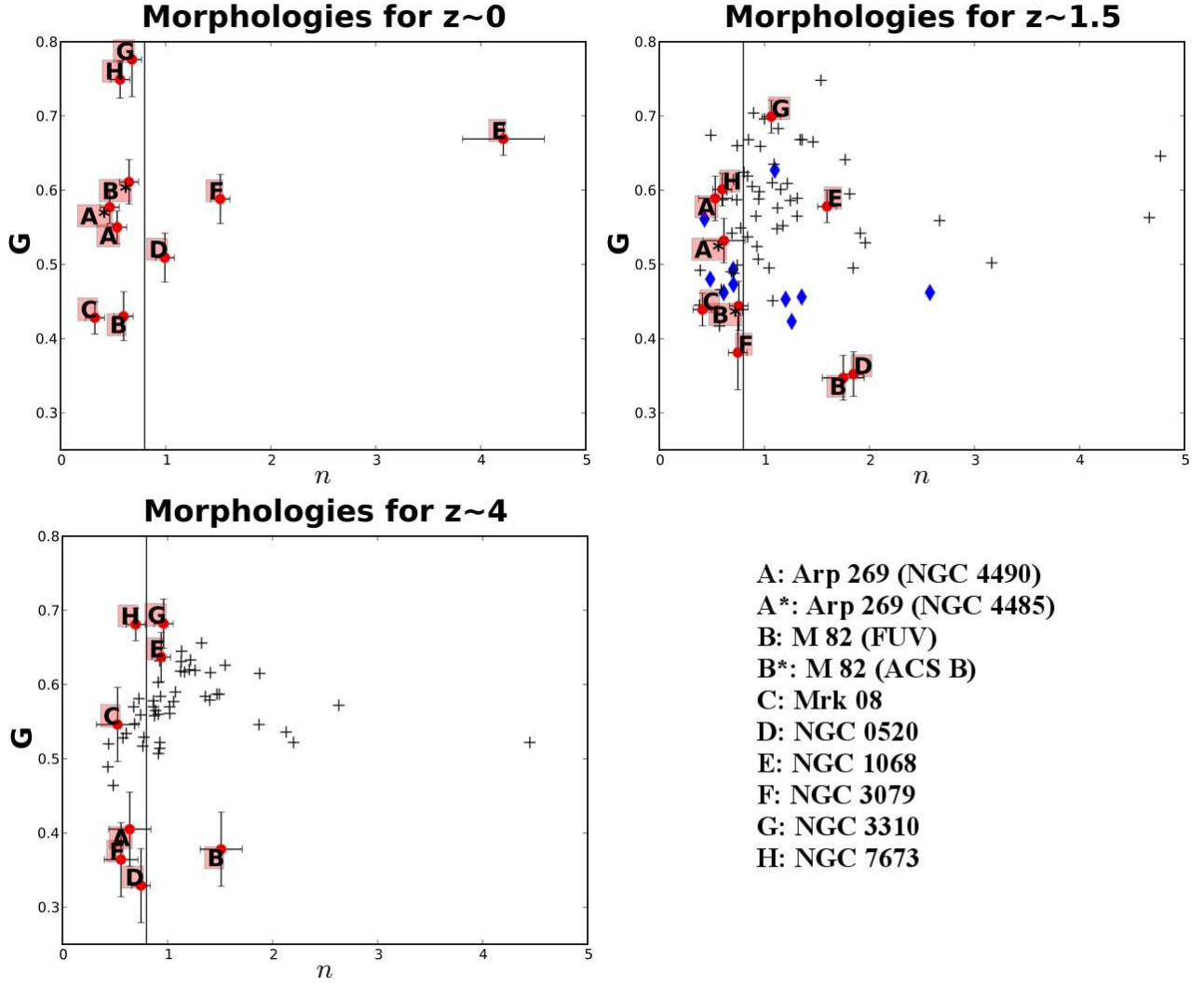


Fig. 7.— We plot G and n , Sérsic index, to determine LBG-like galaxies. The symbols are the same as for Figure 5. The vertical line marks $n = 0.8$, which helps distinguish whether the object, if to the left of the line, has a LBG profile.

TABLE 1
BASIC DATA FOR NEARBY GALAXY SAMPLE^a

Name	Alt. Name	v ^b kms^{-1}	Magnitude ^c B_{Tot}	Morphology	Diameter ^d ''	Luminosity ^e L_{\odot}
Arp 269 (NGC 4490)	UGC 07651	565±3	10.22±.06	SB(s)d pec	6.3	—
Arp 269 (NGC 4485)	UGC 07648	493±7	12.32±.05	IB(s)m pec	2.3	—
M 82	NGC 3034	203±4	9.30±.09	I0:Sbrst	11.2	6.97×10^7
Mrk 08	UGC 03852	3604±8	14.0±.2	I?	0.8	9.42×10^8
NGC 0520	UGC 00966	2281±3	12.24±.13	pec; Sbrst	4.5	2.40×10^8
NGC 1068	M 77	1137±3	9.61±.1	(R)SA(rs)b; Sy1/y2	7.1	1.53×10^9
NGC 3079	UGC 05387	1116±1	11.54±.14	SB(s)c; Sy2	7.9	4.02×10^8
NGC 3310	UGC 05786	993±3	11.15±.1	SAB(r)bc pec	3.1	—
NGC 7673	UGC 12607	3408±1	13.17±.13	(R')SAc? pec	1.3	2.64×10^9

^aNASA/IPAC Extragalactic Database (NED) and RC3 catalogue (de Vaucouleurs et al. 1991)

^bRadial velocity

^cTotal B magnitude

^dMajor axis

^eThe GALEX Ultraviolet Atlas of Nearby Galaxies (Gil de Paz et al. 2007)

TABLE 2
MORPHOLOGIES FOR ARTIFICIALLY REDSHIFTED SAMPLE

Object	G^{z0}	$G^{z1.5}$	G^{z4}	M_{20}^{z0}	$M_{20}^{z1.5}$	M_{20}^{z4}	R_p^{z0}	$R_{p'}^{z1.5}$	R_p^{z4}	n^{z0}	$n^{z1.5}$	n^{z4}
Arp 269 (NGC 4490)	0.55±0.02	0.59±0.03	0.41±0.05	-1.23±0.05	-1.77±0.10	-1.43±0.18	128.0	0.71	0.30	0.54±0.09	0.53±0.16	0.64±0.2
Arp 269 (NGC 4485)	0.58±0.02	0.53±0.03	—	-0.83±0.05	-1.69±0.10	—	47.4	0.50	—	0.47±0.09	0.61±0.20	—
M82 (FUV)	0.43±0.03	0.35±0.03	0.38±0.05	-1.16±0.10	-1.21±0.10	-1.05±0.18	241.2	1.07	0.24	0.60±0.09	1.75±0.20	1.51±0.20
M82 (ACS B ₄₃₅)	0.61±0.03	0.44±0.03	—	-0.94±0.10	-1.40±0.10	—	23.9	1.11	—	0.65±0.09	0.76±0.09	—
Mrk 08	0.43±0.02	0.44±0.02	0.55±0.05	-0.83±0.05	-1.03±0.05	-1.42±0.18	21.8	0.66	0.40	0.33±0.09	0.41±0.09	0.53±0.20
NGC 0520	0.51±0.03	0.35±0.03	0.33±0.05	-0.92±0.10	-0.91±0.10	-1.16±0.18	77.4	1.13	0.46	0.99±0.09	1.85±0.09	0.75±0.09
NGC 1068	0.67±0.02	0.58±0.02	0.64±0.03	-2.43±0.05	-2.06±0.05	-1.76±0.10	26.7	0.56	0.24	4.22±0.39	1.60±0.09	0.94±0.09
NGC 3079	0.59±0.03	0.38±0.05	0.36±0.05	-1.09±0.10	-0.82±0.18	-0.83±0.18	244.3	2.44	1.12	1.52±0.09	0.75±0.09	0.56±0.16
NGC 3310	0.78±0.05	0.70±0.02	0.68±0.03	-1.24±0.18	-1.69±0.05	-1.34±0.10	33.6	0.42	0.25	0.68±0.09	1.07±0.09	0.96±0.09
NGC 7673	0.75±0.02	0.60±0.02	0.68±0.02	-1.18±0.07	-1.43±0.05	-1.46±0.05	17.6	0.42	0.22	0.57±0.09	0.60±0.09	0.70±0.09